Optical parameters estimation in inhomogeneous turbid media using backscattered light: for transcutaneous scattering measurement of intravascular blood

SHIYANG LIANG,[1] ⓘ TAKEO MIYAKE,[1] ⓘ AND KOICHI SHIMIZU[2,*] ⓘ

[1] *Graduate School of Information, Production and Systems, Waseda University, Kitakyushu, 808-0135, Japan*
[2] *School of Optoelectronic Engineering, Xidian University, Xi'an, 710071, China*
*shimizu73@gmail.com

Abstract: In our earlier research, a technique was developed to estimate the effective attenuation coefficient of subcutaneous blood vessels from the skin surface using the spatial distribution of backscattered near-infrared (NIR) light. The scattering effect in surrounding tissues was suppressed through the application of a differential principle, provided that the *in vivo* structure is known. In this study, a new method is proposed enabling the separate estimation of both scattering and absorption coefficients using NIR light of different wavelengths. The differential technique is newly innovated to make it applicable to the subcutaneous structure without requiring explicit geometrical information. Suppression of the scattering effect from surrounding tissue can be incorporated into the process of estimating the scattering and absorption coefficients. The validity of the proposed technique can be demonstrated through Monte Carlo simulations using both homogeneous and inhomogeneous tissue-simulating models. The estimated results exhibit good coherence with theoretical values ($r^2 = 0.988$–0.999). Moreover, the vulnerability and robustness of the proposed technique against different measurement errors are verified. Optimal conditions for practical measurement are specified under various light-detection conditions. Separate estimation of scattering and absorption coefficients improves the accuracy of turbidity measurements and spectroscopy in biomedical applications considerably, particularly for noninvasive measurements and analysis of blood, lipids, and other components in subcutaneous blood vessels.

1. Introduction

Noninvasive measurements of subcutaneous physiological conditions hold important value for biomedical applications [1–3]. The optical properties of body fluids, including blood, lymph, saliva, and cerebrospinal fluid can provide valuable insights into various physiological parameters [4–7]. Among these, the assessment of blood lipid levels has gained rapid importance globally, given the increasing population of overweight people. Temporal changes in serum lipid levels serve as crucially important markers for evaluating overall health in terms of lipid metabolism. Future risks of cardiovascular and diabetes diseases can be predicted based on the lipid metabolism [8,9]. Under healthy conditions, serum lipid levels rise after a meal but revert to normal levels within a few hours. By contrast, abnormal blood metabolism such as postprandial hyperlipidemia engenders sustained high lipid levels until the subsequent meal, consequently increasing the risk of lifestyle-related diseases [10–12]. Currently, diagnosing postprandial hyperlipidemia requires that patients remain in a medical institution for more than several hours for frequent blood sampling [12]. To overcome this limitation, noninvasive optical measurement of blood lipid levels can facilitate continuous real-time evaluation of blood lipid metabolism from the comfort of one's home.

Blood lipids encompass triglycerides (TG), cholesterol, phospholipids, and free fatty acids, with serum TG levels as essential parameters measured in general blood tests. Particularly, TG constitutes a major component of lipoprotein particles such as chylomicrons (CM) and very low-density lipoproteins (VLDL). Because of their larger size than those of other serum lipoproteins, such as low-density lipoproteins (LDL) and high-density lipoproteins (HDL) [13–15], CM and VLDL contribute more to optical scattering from blood. Therefore, serum TG levels can be evaluated using measurements of blood turbidity based on its scattering characteristics [16–18].

For practical measurements of the animal body surface, backscattering measurements are more useful than transmission measurements [19,20]. Many techniques have been developed for measuring the absorption coefficient (μ_a) through backscattering in biomedical applications [4–7,21], but techniques for measuring the scattering coefficient (μ_s) or the reduced scattering coefficient (μ_s') have been used less commonly in medical practice. For an earlier study [22], we proposed an analytical solution to obtain the effective attenuation coefficient (μ_{eff}) of blood, extending the applicability of diffusion approximation to human blood that does not satisfy the scattering-dominant condition. This solution allows the estimation of μ_{eff} from the spatially resolved reflectance observed along the object's surface. When μ_a is known a priori, μ_s' is obtainable from the estimated value of μ_{eff}. However, in real-world scenarios, μ_a might not be known or might vary in time and space.

Furthermore, for our earlier study [22], we developed a technique to suppress the strong light scattering effect in peripheral tissues surrounding the target blood vessel. This technique relies on assumption of the known a priori contribution ratios of the tissue and the blood to the backscattered reflectance. These two assumptions about μ_a and the contribution ratios pose difficult challenges when applying inter-person or in-person comparisons of lipid levels. As described herein, our objective is to advance the noninvasive optical technique for estimating μ_s' and μ_a in a blood vessel while suppressing the scattering effect from peripheral tissues without requiring a priori spatial information about blood vessels.

2. Methods

2.1. Principle of μ_{eff} estimation from backscattering measurements

Light propagation in mammalian tissue is commonly described as energy flow in the equation of transfer. Figure 1 portrays the principle for estimating optical parameters from a reflectance measurement. A vertical narrow beam of light is directed onto the horizontal surface of a scattering object. The backscattered light in the normal direction is measured using a light detector. The reflectance $R(\rho)$ is defined as the intensity ratio between the measured and incident light related to the source–detector distance ρ. In the diffusion approximation to the transfer equation, the reflectance is expressed as shown below [23–25].

$$R(\rho) = \frac{z_0 A_d}{2\pi} \left(\mu_{eff} + \frac{1}{\sqrt{\rho^2 + z_0^2}} \right) \frac{\exp\left(-\mu_{eff}\sqrt{\rho^2 + z_0^2}\right)}{\rho^2 + z_0^2} \tag{1}$$

Therein, $z_0 = 1/\mu_s$' and μ_s'$=(1-g)\mu_s$'. In Eq. (1), μ_s', g, μ_s, A_d and μ_{eff} respectively represent the reduced scattering coefficient, the anisotropy factor, the scattering coefficient of the medium, the detection area and the effective attenuation coefficient. For practical purposes, we can approximate $z_0^2 + \rho^2 \approx \rho^2$ [22]. Consequently, the equation can be transformed as

$$ln[l\rho^2 R(\rho)] = -\mu_{eff}\rho + lln\left(\mu_{eff} + \frac{1}{\rho}\right) + ln\frac{z_0 A_d}{2\pi} \tag{2}$$

Therefore, one can estimate μ_{eff} from the measured reflectance $R(\rho)$ using the slope of the curve $ln[\rho^2 R(\rho)]$ with respect to distance ρ [22,23].
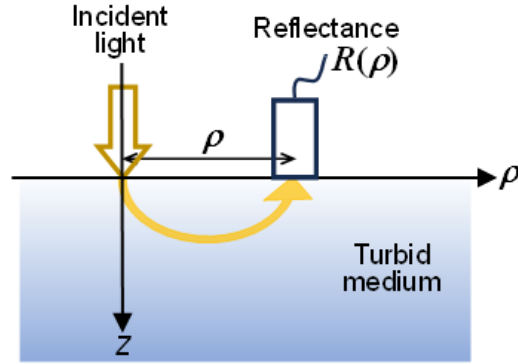
Fig. 1. Model of reflectance measurement.

2.2. Principle of μ_s' and μ_a estimation with two wavelengths

In diffusion approximation, the diffusion coefficient D is given as

$$D = \frac{\mu_a}{\mu_{eff}^2} = [3(\mu_s' + a\mu_a)]^{-1}, \tag{3}$$

where μ_a and a respectively denote the absorption coefficient and the adjusting numerical factor which depends on the form of the diffusion equation [26,27]. When $a = 1$ and 0, Eq. (3) reduces to the classical ($D = [3(\mu_s' + \mu_a)]^{-1}$) and newly proposed ($D = (3\mu_s')^{-1}$) [28] definitions of the diffusion coefficient.

In scattering-dominant cases such as those related to human tissue, the applicability of the diffusion approximation is widely known. However, in the case of whole blood, where the absorption coefficient becomes comparable to the scattering coefficient, the accuracy of the diffusion approximation is not guaranteed. Nevertheless, earlier reports have described that the diffusion approximation still holds in cases where absorption is comparable to scattering if one uses the following factor a [29].

$$a = 1 - \frac{4}{5} \frac{\mu_s' + \mu_a}{\mu_s'(1 + g) + \mu_a} \tag{4}$$

Using Eqs. (3) and (4), the equation for μ_s' and μ_a can be derived as

$$3\mu_a \frac{(5G\mu_s' + \mu_a)(\mu_s' + \mu_a)}{5(G\mu_s' + \mu_a)} = \mu_{eff}^2, \tag{5}$$

where $G = 1 + g$, and μ_{eff} is the value obtained in the reflectance $R(\rho)$ measurement using Eq. (2). In a previous study [22], we obtained μ_s' by solving Eq. (5) as

$$\mu_s' = \frac{-B + \sqrt{B^2 - 4AC}}{2A}, \tag{6}$$

where $A = 15G\mu_a$, $B = 5\,G(3\mu_a^2 - \mu_{eff}^2) + 3\mu_a^2$ and $C = (3\mu_a^2 - 5\mu_{eff}^2)\mu_a$. In this case, the absorption coefficient μ_a was assumed to be known a priori.

However, in practical applications, μ_a is not always known. It might vary with time such as oxygenation changes in hemoglobin. Therefore, the accuracy of μ_s' estimation can be improved if we can estimate μ_a in the same measurement. To estimate μ_a during the μ_s' calculation, we have developed the following new technique.

By conducting the same measurement presented in Fig. 1 using light with two wavelengths λ_1 and λ_2, one can obtain two equations in the form of Eq. (5), which consists of simultaneous equations for unknowns μ_s' and μ_a. However, the number of unknowns also increases as $\mu_s'(\lambda_1)$, $\mu_s'(\lambda_2)$, $\mu_a(\lambda_1)$, and $\mu_a(\lambda_2)$. Often, spectral information about the target material exists, such as blood or body tissue. In such cases, the number of unknowns can be reduced using spectral ratios.

$$\mu_s'(\lambda_2) = k_s \mu_s'(\lambda_1) \tag{7}$$

$$\mu_a(\lambda_2) = k_a \mu(\lambda_1) \tag{8}$$

In these equations, k_s and k_a respectively stand for the spectral ratios of molar scattering and absorption coefficients $\varepsilon_s(\lambda_1)/\varepsilon_s(\lambda_2)$ and $\varepsilon_a(\lambda_1)/\varepsilon_a(\lambda_2)$. Consequently, we obtain the simultaneous equations for two unknowns, μ_s' and μ_a of wavelength λ_1, as shown below.

$$\begin{cases} 3\mu_a \frac{(5G\mu_s'+\mu_a)(\mu_s'+\mu_a)}{5(G\mu_s'+\mu_a)} = \mu_{eff}^2(\lambda_1) \\ 3k_a\mu_a \frac{(5Gk_s\mu_s'+k_a\mu_a)(k_s\mu_s'+k_a\mu_a)}{5(Gk_s\mu_s'+k_a\mu_a)} = \mu_{eff}^2(\lambda_2) \end{cases} \tag{9}$$

Therein, $\mu_s' = \mu_s'(\lambda_1)$ and $\mu_a = \mu_a(\lambda_1)$.

2.3. Convenient method for μs' and μa estimation

Various approaches exist for solving Eq. (9). A simple technique is numerical two-parameter estimation. Among them, we chose a simple technique by which we can observe the behaviors of estimated μ_s' and μ_a directly. Because each equation in Eq. (9) is quadratic with respect to μ_s', Eq. (9) can be transformed to the expression shown below.

$$\begin{cases} \mu_s' = \frac{-5G(3\mu_s^2-\mu_{eff}1^2)-3\mu_a^2+\sqrt{[5G(3\mu_a^2-\mu_{eff}1^2)+3\mu_a^2]^2-60G\mu_a^2(3\mu_a^2-5\mu_{eff}1^2)}}{30G\mu_a} \\ \mu_s' \frac{-5G(3k_a^2\mu_a^2-\mu_{eff}2^2)-3k_a^2\mu_a^2+\sqrt{[5G(3k_a^2\mu_a^2-\mu_{eff}2^2)+3k_a^2\mu_a^2]^2-60Gk_a^2\mu_a^2(3k_a^2\mu_a^2-5\mu_{eff}2^2)}}{30Gk_sk_a\mu_a} \end{cases} \tag{10}$$

Therein, $\mu_{eff1} = \mu_{eff}(\lambda_1)$ and $\mu_{eff2} = \mu_{eff}(\lambda_2)$. Each equation in Eq. (10) yields μ_s' as a function of known G, k_s, k_a, measured μ_{eff1}, μ_{eff2} and one unknown μ_a. If unknown μ_a is the correct value, then both equations will result in the same μ_s'. Therefore, we can ascertain the correct μ_a in the search for the minimum difference in the two μ_s' values calculated in Eq. (10). To evaluate this difference, we use the Michelson contrast, defined as

$$C_M = \frac{\mu_s'|_f - \mu_s'|_l}{\mu_s'|_f + \mu_s'|_l}, \tag{11}$$

where C_M, $\mu_s'|_f$ and $\mu_s'|_l$ respectively represent the Michelson contrast, with μ_s' obtained in the former and the latter equations in Eq. (10). An example of the dependence of these parameters on μ_a is presented in Fig. 2. $\mu_s'|_f$ and $\mu_s'|_l$ change at different rates with μ_a crossing at a certain point. The contrast becomes minimum at the specific value of μ_a. This μ_a and the corresponding μ_s' are the solutions of the simultaneous equation Eq. (9) or Eq. (10).

Based on the principle presented above, we can estimate μ_s' and μ_a using the following process. Figure 3 presents an example of the process in a flow chart. Initially, we calculate both equations in Eq. (10) with an assumed initial value of μ_a. After validating the calculated μ_s', we compare them using contrast C_M. If any μ_s' falls outside the valid range or if the contrast is insufficiently small, then we update the value of μ_a. By repeating this process until the contrast value becomes smaller than the preset threshold, we can estimate μ_s' and μ_a using the same procedure.

In this process, it is necessary to update the μ_a value to minimize contrast C_M. The Newton–Raphson method is one candidate for achieving convergence. The stability of this
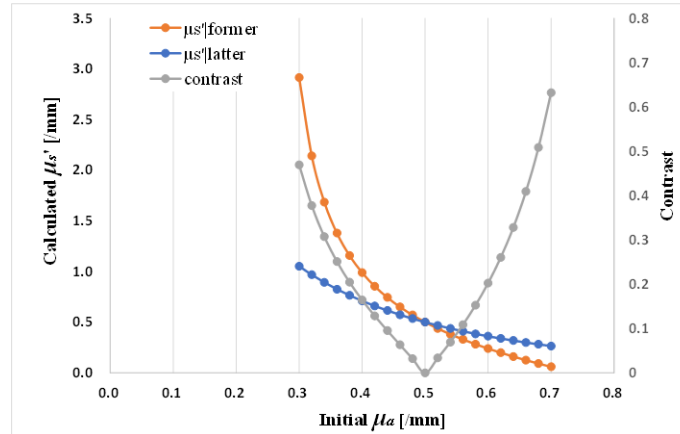
Fig. 2. Dependence of reduced scattering coefficient μ_s' in two solutions and its contrast on absorption coefficient μ_a: $\mu_{eff1} = 1.046$ /mm, $\mu_{eff2} = 2.250$ /mm, $g = 0.99$, $k_s = 0.647$, and $k_a = 3.80$ (assuming practical wavelengths $\lambda_1 = 660$ nm and $\lambda_2 = 940$ nm).
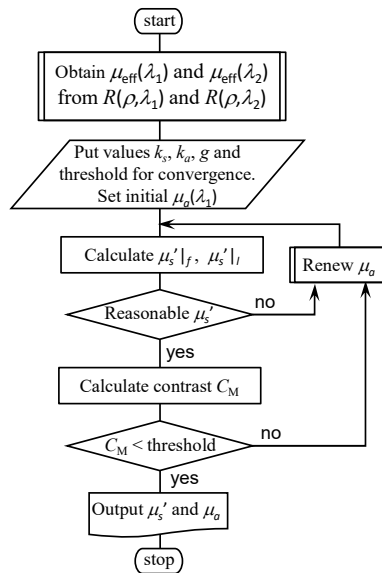
**Fig. 3.** Process for μ_s' and μ_a separated estimation: μ_{eff} is estimated from the $\ln[\rho^2 R(\rho)]$ curve with respect to ρ using Eq. (2). μ_a is updated to achieve convergence in the contrast C_M.

convergence process has been confirmed when starting with reasonable initial values of μ_a reported in the literature [4–7,25]. An important feature of this process is the direct testability of the estimated μ_s' and μ_a values during the convergence process. During the process of μ_s' calculation, we examine the validity of μ_s' to ensure that the value falls within an appropriate range. We can also confirm the validity of μ_a during its updating process. This feature supports calculation efficiency by eliminating unnecessary calculations of erroneous cases.

2.4. Application of the differential method

The primary objective of this study is the noninvasive measurement of blood in a subcutaneous blood vessel using the reflectance $R(\rho)$ measured at the body surface. Figure 4 illustrates the reflectance measurement at the body surface with a subcutaneous blood vessel.
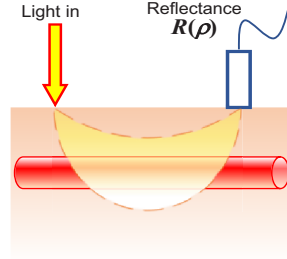
Fig. 4. Reflectance measurement with subcutaneous blood vessel.

The probing volume intersects not only the blood vessel but also the surrounding tissue. Consequently, the reflectance $R(\rho)$ is inevitably influenced more by the optical properties of the surrounding tissue than by those within the blood vessel. To evaluate μ_s' and μ_a within the blood vessel, considering the surrounding tissue's strong effect, we developed a technique using a differential principle between the reflectances with and without the blood vessel [22]. Figure 5 portrays the measurement setup used for this technique. Reflectances were measured on the body surface along lines just above the blood vessel axis and off the axis. The contribution of the blood vessel component to the reflectance can be differentiated from that of the body tissue using the following equations.

$$R_{\text{on}}(\rho) = \alpha(\rho) R_{blood}(\rho) + [1 - \alpha(\rho)] R_{tissue}(\rho)$$
$$R_{\text{off}}(\rho) = \beta(\rho) R_{blood}(\rho) + [1 - \beta(\rho)] R_{tissue}(\rho)$$

(12)
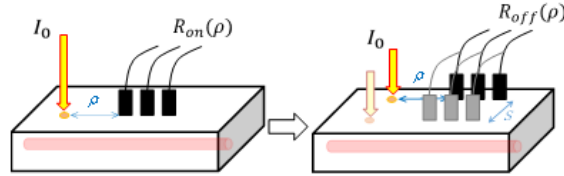
Fig. 5. Measurement of on-axis and off-axis reflectances for differential technique to suppress scattering effect from surrounding tissue: I_0 and s respectively denote the incident light intensity and the shift distance.

In those equations, $R_{\text{on}}(\rho)$ and $R_{\text{off}}(\rho)$ respectively represent the on-axis and off-axis reflectances. Therein, $\alpha(\rho)$ and $\beta(\rho)$ respectively denote the contribution factors of the blood vessel component to the reflectances $R_{\text{on}}(\rho)$ and $R_{\text{off}}(\rho)$. This technique can also be employed for the multi-wavelength estimation method proposed in this study. The reflectance of blood in the blood vessel is given as presented below.

$$R_{blood}(\rho, \lambda) = \frac{[1 - \beta(\rho, \lambda)]R_{\text{on}}(\rho, \lambda) - [1 - \alpha(\rho, \lambda)]R_{\text{off}}(\rho, \lambda)}{\alpha(\rho, \lambda) - \beta(\rho, \lambda)}$$

(13)

The effectiveness of this technique depends on the appropriate choice of the contribution factors. Here, $\alpha(\rho, \lambda)$ and $\beta(\rho, \lambda)$ are determined uniquely in Monte Carlo simulations using
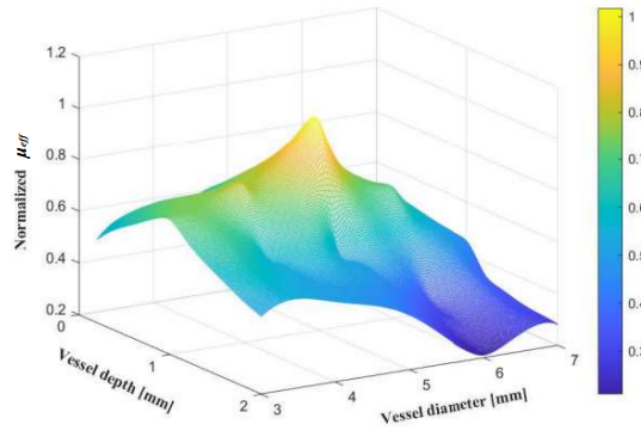
Fig. 6. Characteristics of μ_{eff} for variation of assumed depth and diameter of blood vessel in body tissue. Vertical axis is the estimated μ_{eff} value normalized by the value for true geometry. (Tissue: μ_s'=1.0/mm, μ_a = 0.01/m. Blood: μ_s'=0.5/mm, μ_a = 0.5/mm. Detector array shift: s = 5.0 mm, True depth d = 1 mm. True diameter ϕ=5 mm)

depth d and diameter ϕ of the blood vessel in the body tissue. In our earlier study, d and ϕ were assumed to be known a priori [22]. However, in real measurements with human subjects, they are often unknown. Additionally, the vessel diameter can vary depending on the physiological and psychological conditions of the subject. To find appropriate contribution factors, we developed a new technique to estimate d and ϕ during the μ_s' and μ_a estimation process.

The principle of this choice is based on a database search. First, we prepare a database of contribution factors $\alpha(\rho)$ and $\beta(\rho)$ for different combinations of optical and geometrical parameters, i.e., μ_s', μ_a, d, and ϕ. The database provides output (α, β) for given input of $(\mu_s$', $\mu_a, d, \phi)$. When some input parameters are unknown, we scan the unknown parameters within a practically reasonable range, resulting in multiple candidate sets of (α, β) outputs. We then select the appropriate contribution factors from these candidates. Optical parameters μ_s' and μ_a can be estimated using the different methods described in earlier sections 2.2 and 2.3. Therefore, we typically scan the geometrical parameters d and ϕ.

Among the candidate sets of (α, β) outputs, an appropriate contribution factor set is identifiable by choosing the one which results in the steepest slope of $R_{blood}(\rho)$, leading to the maximum μ_{eff}. This principle is derived from large difference in light absorption between blood and body tissue. In the NIR wavelength range, the values of $(\mu_s$', $\mu_a)$ are typically in the orders of (0.5/mm, 0.5/mm) and (1.0/mm, 0.01/mm), respectively, for blood and body tissue. Considering Eq. (3), or $\mu_{eff} = [3\mu_a(\mu_s$'$+a\mu_a)]^{1/2}$, the value of μ_{eff} for blood is much larger than that of body tissue. Therefore, we can select the appropriate contribution factors as the set that results in the maximum μ_{eff}. Figure 6 presents μ_{eff} estimated from the reflectance $R_{blood}(\rho)$ calculated using $R_{on}(\rho)$, $R_{off}(\rho)$, $\alpha(\rho)$, and $\beta(\rho)$ for assumed d and ϕ. It shows a typical distribution with a single peak at the correct d and ϕ. This unimodal change enables us to obtain the required appropriate contribution factors.

This database approach is akin to the neural network trained with Monte-Carlo simulation data [21]. While the neural network technique offers greater flexibility and versatility for general applications, the proposed technique is straightforward and can be easily implemented in the system described in the following section.
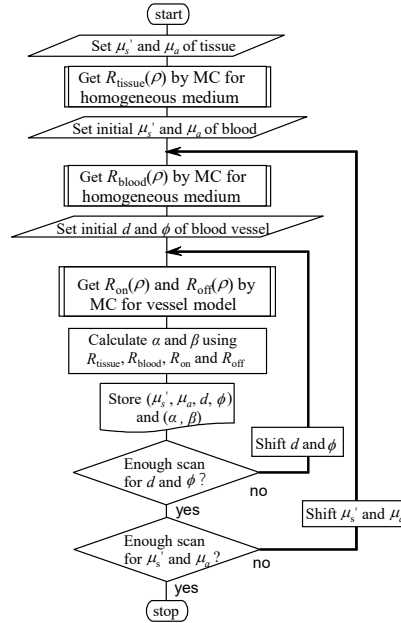
Fig. 7. Process of creating database to obtain contribution factors from given optical and geometrical conditions of turbid medium: $R_{\text{tissue}}(\rho)$, $R_{\text{blood}}(\rho)$, $R_{\text{on}}(\rho)$, and $R_{\text{off}}(\rho)$ are obtained from Monte Carlo simulation of photon migration as the ratio of received photon energy at the source–detector distance ρ. The contribution factors $\alpha(\rho, \lambda)$ and $\beta(\rho, \lambda)$ are calculated using Eq. (14). This database provides output (α, β) for the input (μ_s', μ_a, d, ϕ).

2.5. Integration into a system

The proposed techniques were integrated into a system consisting of a database and data-processing algorithms. Figure 7 depicts the process of creating the database, which can output the contribution factors $\alpha(\rho, \lambda)$ and $\beta(\rho, \lambda)$ for given optical and geometrical parameters, i.e., μ_s', μ_a, d and ϕ. In this database generation, $\alpha(\rho, \lambda)$ and $\beta(\rho, \lambda)$ are calculated using reflectances of four kinds obtained from Monte Carlo simulations of photon migration in a turbid medium [22,30] as

$$\alpha\left(\rho, \lambda\right) = \left[R_{\text{tissue}}\left(\rho, \lambda\right) - R_{\text{on}}\left(\rho, \lambda\right)\right] / \left[R_{\text{tissue}}\left(\rho, \lambda\right) - R_{\text{blood}}\left(\rho, \lambda\right)\right]$$
$$\beta\left(\rho, \lambda\right) = \left[R_{\text{tissue}}\left(\rho, \lambda\right) - R_{\text{off}}\left(\rho, \lambda\right)\right] / \left[R_{\text{tissue}}\left(\rho, \lambda\right) - R_{\text{blood}}\left(\rho, \lambda\right)\right]$$
(14)

where $R_{\text{on}}(\rho, \lambda)$ and $R_{\text{off}}(\rho, \lambda)$ represent the reflectances measured at the body surface along and off the axis of the subcutaneous blood vessel, respectively. $R_{\text{tissue}}(\rho, \lambda)$ and $R_{\text{blood}}(\rho, \lambda)$ correspond to the reflectances of tissue and blood in a homogeneous structure.

Figure 8 shows the data-processing algorithm used to estimate μ_s' and μ_a of the blood in the subcutaneous blood vessel with unknown depth and diameter using the reflectances $R_{\text{on}}(\rho)$ and $R_{\text{off}}(\rho)$ measured on the body surface.
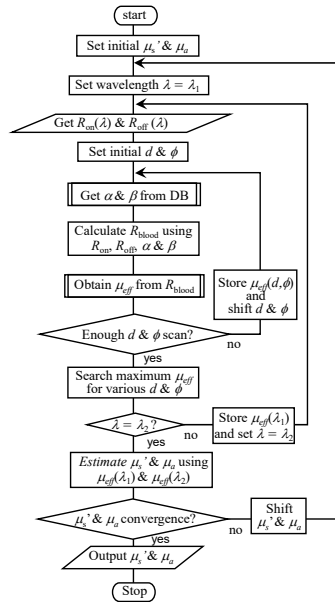
Fig. 8. Overall process to estimate μ_s' and μ_a of the blood in the blood vessel with unknown depth and diameter in body tissue: Contribution factors α and β are obtained from the database (DB) prepared using the process depicted in Fig. 7. μ_{eff} is estimated from the $\ln[\rho^2 R(\rho)]$ curve with respect to ρ using Eq. (2). Here, μ_s' and μ_a are estimated in the process depicted in Fig. 3.

3. Validity check of the proposed technique

3.1. Conditions of simulation

Figure 9 depicts the model used for the Monte Carlo simulation [22,30–32] to assess the validity of the proposed technique. To simulate the case with a subsurface vein in the forearm of an adult human, the depth and diameter of the blood vessel were set at $d = 1.0$ mm and $\phi = 5.0$ mm, respectively, based on fundamental conditions. Light detecting areas were arranged as small squares aligned in the x-direction along the horizontal surface of a turbid medium. These squares were 1 mm × 1 mm, with centers at $\rho = 1, 2, 3\ldots$ mm. The reflectance $R(\rho)$ was obtained as the integrated photon energy backscattered from the medium and detected in each area. All photons that reached the detection-square from any angle in the half-space were counted as detected photons.

For a homogeneous medium, the optical parameters of the blood vessel part were set to be the same as those of the surrounding tissues. With practical application to blood turbidity measurements in mind, the wavelengths were set as $\lambda_1 = 660$ nm and $\lambda_2 = 940$ nm. The optical parameters of blood were varied: $\mu_s'(\lambda_1) = 0.1$–2.0 mm^{-1}, $\mu_a(\lambda_1) = 0.1$–0.9 mm^{-1} with $k_s = 0.647$, $k_a = 3.80$, and $g = 0.99$ at both wavelengths. Meanwhile, the parameters of tissue were $\mu_s' = 1.0$ mm^{-1}, $\mu_a = 0.01$ mm^{-1} and g = 0.95 at both wavelengths [33–37]. Reflectances $R_{blood}(\rho, \lambda)$ and $R_{tissue}(\rho, \lambda)$ were obtained, respectively, from the simulation for homogeneous media with optical parameters corresponding to blood and body tissue. Also, $R_{on}(\rho, \lambda)$ and $R_{off}(\rho, \lambda)$ were obtained along the on-axis and off-axis lines above the blood vessel with a shift distance $s = 5.0$ mm. The validity of this model was confirmed by comparing it with experimental data [22].
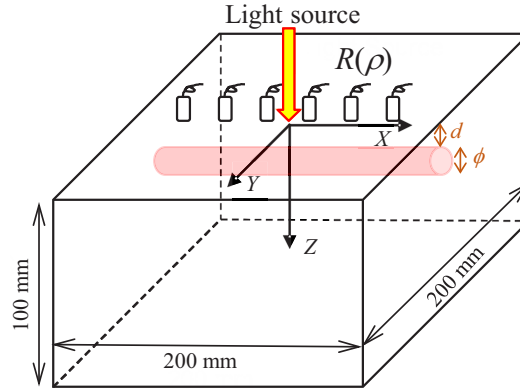
Fig. 9. Model for Monte Carlo simulation: Photons are injected at the center of the upper surface. After propagation in the medium, backscattered photons are received as reflectance $R(\rho)$ as a function of the radial distance ρ from the light incidence point. A blood vessel with a diameter ϕ is located at a depth d below the surface.

All the Monte-Carlo simulations were executed on a computer equipped with Intel Xeon Gold 6348 CPU (2.60 GHz, 256GB). The typical runtime for a single set of reflectance calculation was about 260000 seconds.
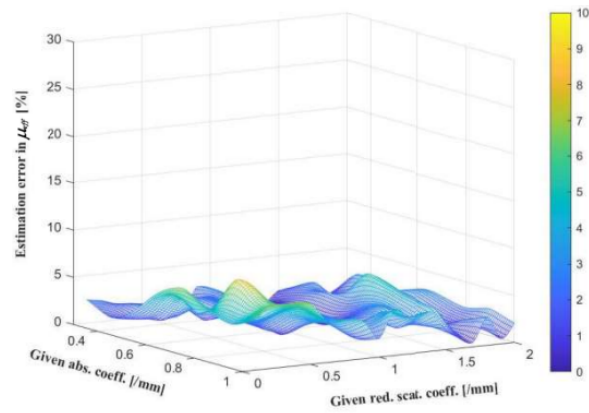
3.2.　Accuracy in a homogeneous medium

The absorption coefficient μ_a of the blood is of the same order as the reduced scattering coefficient, which does not satisfy the conditions of the diffusion approximation. Because Eq. (2) was derived from diffusion approximation, its accuracy in estimating μ_{eff} is not guaranteed, especially for blood. From simulation and experimentation, we verified that this technique became applicable by adjusting factor a in Eq. (4), even in the case of blood [22]. However, the effectiveness of Eq. (6) for scattering estimation was only examined with a known absorption coefficient μ_a. Therefore, for the current study, we examined the validity of the newly proposed technique to estimate both the reduced scattering coefficient μ_s' and the absorption coefficient μ_a simultaneously in a homogeneous medium including non-scattering-dominant conditions.

Reflectances $R(\rho, \lambda_1)$ and $R(\rho, \lambda_2)$ were obtained in the Monte Carlo simulation of photon migration in a scattering medium. Using Eq. (2), we estimated $\mu_{eff}(\lambda_1)$ and $\mu_{eff}(\lambda_2)$ respectively from $R(\rho, \lambda_1)$ and $R(\rho, \lambda_2)$. Also, μ_s' and μ_a for λ_1 were estimated using Eq. (10) in the process depicted in Fig. 3. The estimation error was evaluated as the percentage error, i.e., the absolute value of the difference between the estimated and given values normalized by the given value.

The estimation errors for different combinations of given μ_s' and μ_a are shown in Fig. 10. Although some estimation errors are unavoidable because of reasons such as the reflectance at discrete detection points and the randomness in Monte Carlo simulation, most of them remained below a few percent for μ_{eff}, and below several percent for μ_s' and μ_a. These results verify the validity of the proposed technique for μ_s' and μ_a estimation in homogeneous media with a non-scattering-dominant condition, such as blood.
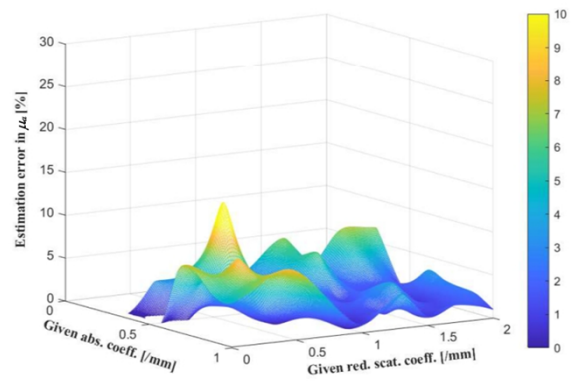
3.3.　Effectiveness of the differential technique

In the newly proposed technique, the estimation of μ_{eff} from $R(\rho)$ serves as the basis for estimating μ_s' and μ_a in the blood vessel. Reflectance $R(\rho)$ should represent the blood rather than the surrounding tissue. However, as depicted in Fig. 4, the probing volume intersects not only the blood vessel but also the surrounding tissue. Therefore, the reflectance measured on the body surface is inevitably masked by the overwhelming effect of tissue reflectance. The effectiveness

(a)
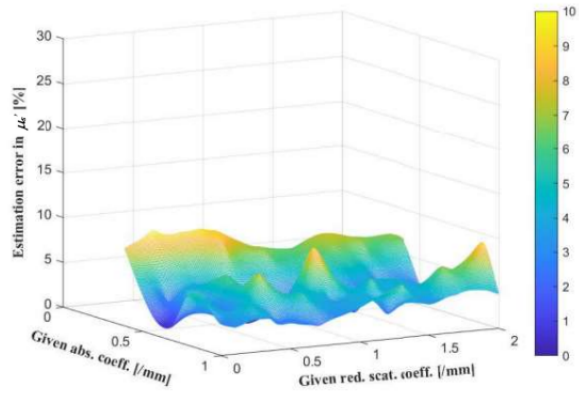
(b)

(c)

Fig. 10. Estimation error in a homogeneous medium: (a) effective attenuation coefficient, (b) reduced scattering coefficient, and (c) absorption coefficient.

of the proposed differential technique was examined in the simulation to estimate μ_{eff} from the reflectance $R(\rho)$ obtained in the process of Section 3.1.

Figure 11 presents results of μ_{eff} estimation obtained when both μ_s' and μ_a in the subcutaneous blood vessel are varied. The estimated μ_{eff} exhibits a linear dependence on the given μ_{eff}, even without the differential technique. This finding verifies the fundamental feasibility of noninvasive measurement to detect changes in optical properties inside the human body. However, the low slope of the regression line represents very low sensitivity. The change in the blood vessel was masked by the constant optical parameters of the surrounding tissue. This masking effect was suppressed using the differential technique. In fact, using the differential technique, the sensitivity increased by about 10 times. The estimated values became more reliable. Based on these results, the differential technique was used for the following analyses.
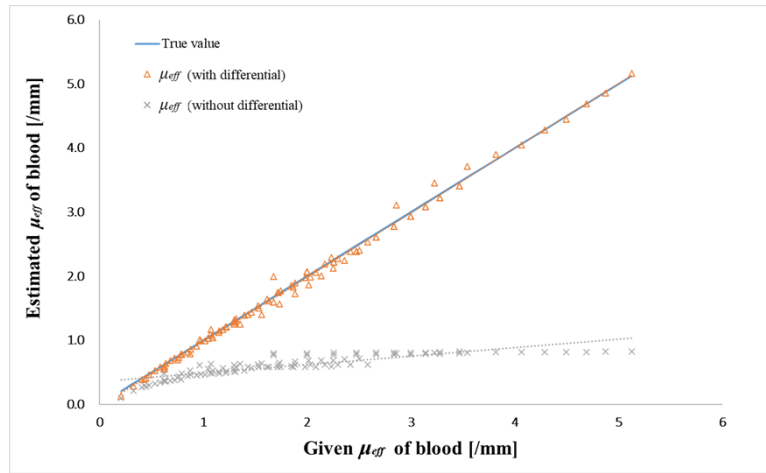

Fig. 11. Effectiveness of differential technique in estimating μ_{eff} of blood in blood vessel by eliminating the influence of surrounding tissues. (Tissue: μ_s'=1.0/mm, μ_a = 0.01/m. Blood: μ_s'=0.1–2.0/mm, μ_a = 0.3–1.0/mm. Detector array shift: s = 5.0 mm. Blood vessel depth d = 1.0 mm. Blood vessel diameter ϕ=5.0 mm)

3.4. Accuracy in the blood vessel

The on-axis and off-axis reflectances $R_{\text{on}}(\rho, \lambda)$ and $R_{\text{off}}(\rho, \lambda)$ were obtained for two wavelengths $\lambda_1 = 660$ nm and $\lambda_2 = 940$ nm in the Monte Carlo simulation with the model presented in Fig. 9. Because the wavelength variations of μ_s' and μ_a of surrounding tissue are markedly less than those in blood vessel, the optical parameters for surrounding tissues were set as μ_s'= 1.0 mm^{-1}, μ_a = 0.01 mm^{-1} with g = 0.95 for both wavelengths λ_1, and λ_2. Parameters within the blood vessel were varied in the ranges of μ_s'= 0.1–2.0 mm^{-1}, and μ_a = 0.1–0.9 mm^{-1} with g = 0.99. These values were selected based on reported values [4–7,33–37]. Using the process portrayed in Fig. 8, μ_s' and μ_a were estimated.

Figure 12 presents the accuracy of the proposed technique. The average values over the variation of another parameter are shown as the mean values with error bars representing the standard deviations, i.e., $m \pm \sigma$. Good agreement can be observed between the given and estimated values, with small variations in both μ_s' and μ_a estimation. These results also verify the validity of the proposed technique for the separate estimation of μ_s' and μ_a in a localized part of a turbid medium, such as the blood vessel in the surrounding tissue.

We can expect higher accuracy for a larger vessel at a shallower depth, as it closely approximates the conditions of a homogeneous medium. However, as the vessel becomes smaller and deeper,
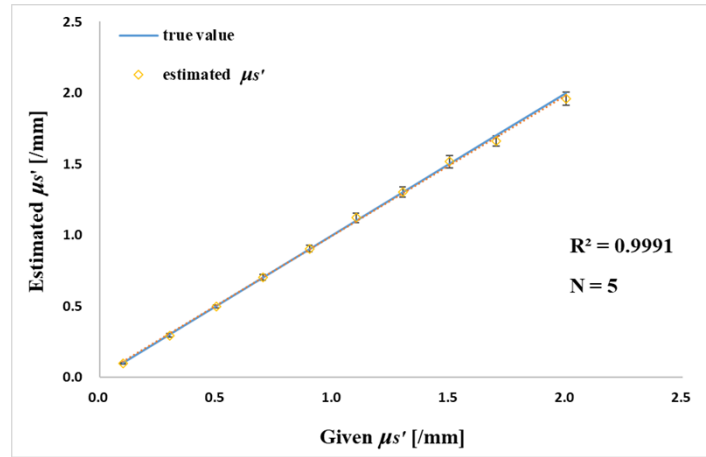
(a)
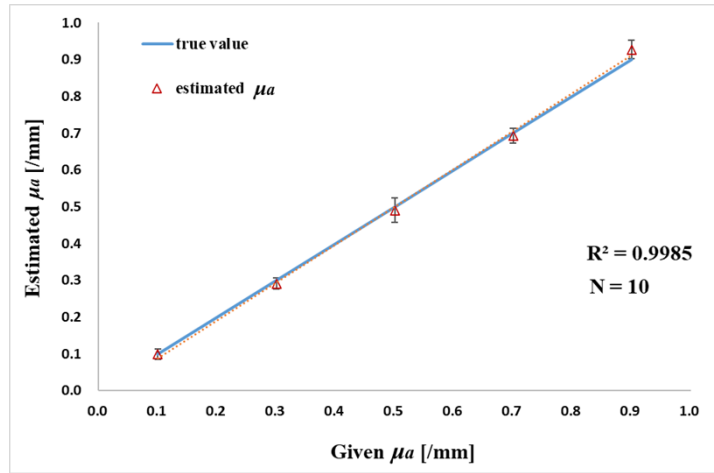
(b)

Fig. 12. Results of separate estimation of μ_s' and μ_a: (a) estimated μ_s' over μ_a variation ($N = 5$), (b) estimated μ_a over μ_s' variation ($N = 10$); The optical parameters of tissue and blood are respectively (μ_s' = 1.0/mm, μ_a = 0.01/mm) and (μ_s' = 0.1–2.0/mm, μ_a = 0.1–0.9/mm). The detector-array shift, the blood vessel depth, and the blood vessel diameter were, respectively, 5.0 mm, 1.0 mm and 5.0 mm.

the accuracy becomes lower because the cross-sectional area between the probing volume and the vessel becomes smaller.

4. Practical considerations for application

4.1. Vulnerability and tolerance against measurement noise

The proposed technique can be regarded as an inverse problem aimed at inferring the cause (μ_s' and μ_a) from the result ($R(\rho)$). In inverse problems, even slight noise in the measured $R(\rho)$ can engender non-negligible error in the estimation of μ_s' and μ_a. To investigate this possibility,

random noise of various types was added to the reflectance $R(\rho)$. The resulting estimation errors were analyzed.

The reflectance values were varied using the following equations to simulate random noise and bias noise.

$$R_r(\rho) = [1 + (RN-0.5)W]R_{MC}(\rho) \tag{15}$$

$$R_b(\rho) = R_{MC}(\rho) + WR_{max}. \tag{16}$$

In those equations, $R_r(\rho)$, $R_b(\rho)$, and $R_{MC}(\rho)$ respectively represent reflectances with random noise, with bias noise, and the noise-free reflectance obtained from Monte Carlo simulation. Also, R_{max} is the maximum reflectance value in the measurement range of ρ. RN and W respectively denote a random number between 0.000 and 1.000 and the weight for noise amplitude. Figure 13 presents the results of the error analysis in the form of mean values with error bars representing the standard deviations, i.e., $m \pm \sigma$. N corresponds to the μ_a and μ_s' variations in μ_s' and μ_a estimation, respectively.
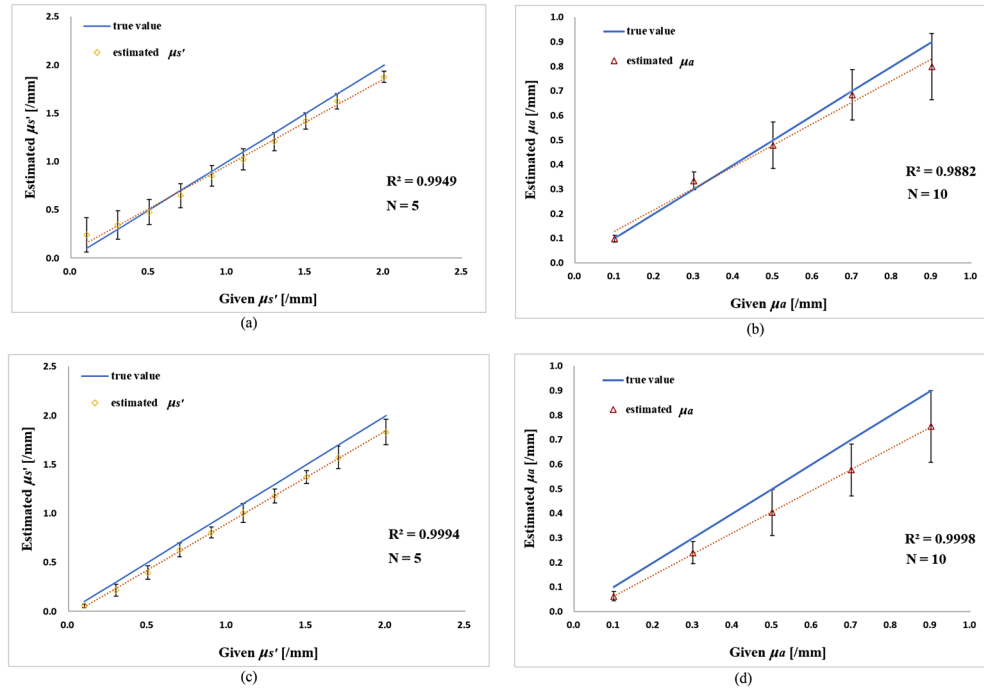

Fig. 13. Results of error-analysis for separated estimation of μ_s' and μ_a: (a) estimated μ_s' over μ_a variation with 20% random noise ($N = 5$, $W = 0.2$) in reflectance measurement, (b) estimated μ_a over μ_s' variation with 20% random noise ($N = 10$, $W = 0.2$), (c) estimated μ_s' over μ_a variation with 20% bias noise ($N = 5$, $W = 0.2$), and (d) estimated μ_a over μ_s' variation with 20% bias noise ($N = 10$, $W = 0.2$).

As shown in Figs. 13(a) and 13(c), the μ_s' estimation error remains in the same order as the noise in reflectance measurement. This robustness apparently arises from the principle of μ_{eff} estimation. Because μ_{eff} is estimated from the slope of reflectance $R(\rho)$, the fluctuation attributable to noise can be averaged out in the slope detection. This averaging effect is more effective for random noise than for bias noise. The bias noise raises the reflectance value more in a larger ρ range, where the reflectance value is smaller, resulting in reducing the slope of the reflectance. The slope reduction engenders lower μ_{eff} estimation. This finding explains the slight underestimation observed in Fig. 13(c).

Regarding μ_a estimation in Figs. 13(b) and 13(d), a non-negligible error was observed in the range $\mu_a > 0.7$. This result suggests the noise-susceptibility of this technique in the measurement of high absorption values. However, the mean estimated values showed strong correlation with the given values, and the error remained in the same order as that of the noise in reflectance measurements. These results verify the applicability of the proposed technique for μ_s' and μ_a estimation in practical applications.

4.2. *Accuracy dependence on the detection range*

When a narrow beam of light is directed onto a turbid medium, the incident light disperses extensively after propagating a mean-free-path length, typically around 1 mm for NIR light in human body tissue [4–7,38–41]. The backscattered light is detected by a detector. Even when the detector's receiving angle is small, its detection volume also significantly expands in the medium due to intense light scattering. The probing volume of the backscattered light with the detector is obtained as the superposition of these two spreads [42,43]. Figure 14(a) portrays the variation of this probing volume with the detector position.
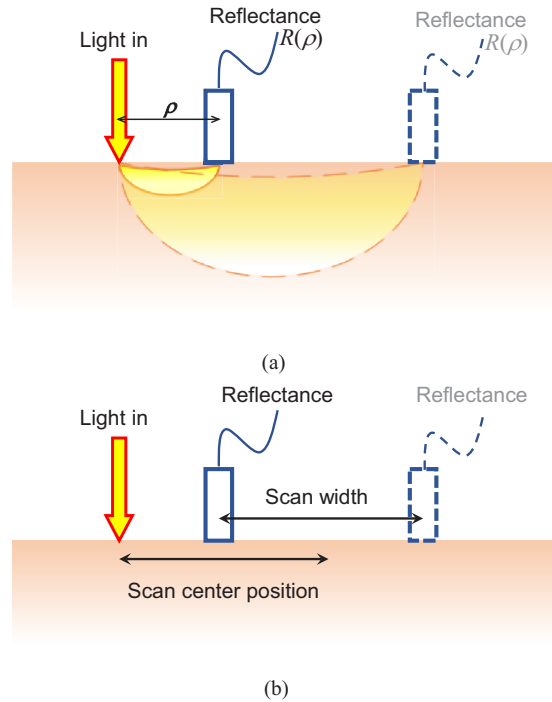

Fig. 14. Measurement of reflectance by scanning the medium's surface with a photodetector: (a) variation in probing volume, (b) measurement with a variable detection range.

Using the proposed technique, we estimate μ_s' and μ_a from reflectance $R(\rho)$ measured as a function of the source–detector distance ρ. The diffusion approximation is applicable when $\rho >> 1/\mu_s$'. The backscattered light intensity is less than that of the diffusion approximation in the range of less than a few millimeters [22]. If ρ is set as too small, then estimation based on the diffusion approximation becomes erroneous. By contrast, large ρ guarantees the accuracy of the diffusion approximation. However, as ρ becomes large, the backscattered light intensity drops rapidly below the detection limit. Moreover, for accurate measurement of the slope of $\ln(\rho^2 R)$, the reflectance $R(\rho)$ should be measured over widely various ρ. Nevertheless, this

wide range will inevitably include inappropriate positions at either side of the range, leading to potential inaccuracies. Therefore, we analyzed the dependence of the estimated μ_{eff} accuracy on the ρ-range to identify appropriate conditions for the estimation of μ_s' and μ_a of the blood.

Figure 15 presents the result of the error analysis for a homogeneous blood case, where μ_s' $=\mu_a = 0.5$ /mm. The two axes in the horizontal plane correspond to the center coordinate and the width of the detector scan (ρ-range), as portrayed in Fig. 14(b). The ranges of these two axes were chosen considering the practical measurement conditions. The error became smaller with the center position of the ρ-range, indicating an increase in the accuracy of the diffusion approximation. Regarding the ρ-range width, the error remained low in 1–10 mm width range and increased gradually in the 10–20 mm width range. This increase was attributed to the inclusion of inappropriate detector positions. Moreover, this tendency was apparent when the center position was less than 6 mm. Results obtained from this analysis suggest that the position and width of the light detection range should be chosen carefully to ensure accurate measurements.
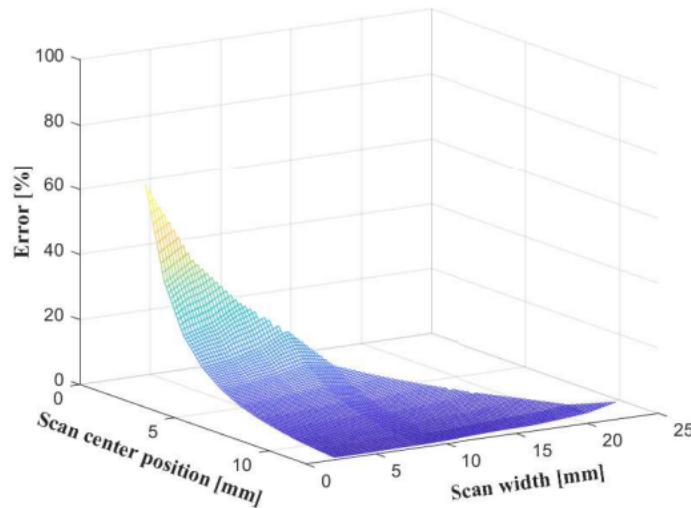
Fig. 15. Error analysis for appropriate detection range of reflectance measurement: μ_s' $=\mu_a = 0.5$ /mm. Vertical axis is the percent error in μ_{eff} estimation.

5. Discussion

We have developed a noninvasive technique to acquire optical properties of a localized part in a turbid medium, such as blood turbidity in blood vessels. One crucially important issue encountered during the measurement of subcutaneous blood vessels was the strong scattering effect from surrounding body tissue. We can suppress this effect using the differential principle between reflectances with and without the blood vessel. However, to apply this principle, geometrical information of the blood vessel must be obtained. To address this challenge, we introduced a new technique based on the differential principle to suppress the scattering effect without prior knowledge of the blood vessel geometry. By leveraging prior learning or database preparation, we were able to reduce the strong scattering effect from tissues surrounding the target blood vessel. To streamline the estimation processes, we integrated the μ_s' and μ_a estimation and the differential operation into a single algorithm.

Through extensive computer simulations, we examined the feasibility and characteristics of the proposed technique. We validated the accuracy of μ_s' and μ_a estimation specifically for non-scattering-dominant media like the blood in subcutaneous blood vessels. Although it was possible to detect changes in μ_{eff} without employing the differential technique, we observed

limited sensitivity resulting in estimated values that were markedly smaller than the true values. However, with application of the differential technique, sensitivity improved approximately ten-fold, leading to estimated values that closely approached the true ones. Our error analysis confirmed that the estimation error in μ_s' and μ_a estimation remained below 10% within the practical range of human blood measurement.

Because μ_s' and μ_a estimation from the measured reflectance constitutes an inverse problem, the estimation error attributable to measurement noise might reach unrealistic magnitudes. To assess the susceptibility of the proposed technique against measurement noise, random noise and bias noise were added to the measured reflectance. Then μ_s' and μ_a were estimated. Because of the averaging function in the process of μ_{eff} estimation, the estimation errors did not escalate beyond the magnitude of measurement noise. This robustness against measurement noise highlights an important benefit of our proposed technique, particularly for practical applications.

Additionally, we analyzed the dependence of accuracy on the radial range of reflectance measurement to maximize the effectiveness of the proposed technique. Our analysis revealed that a suitable radial range (i.e. $\rho = 6$–16 mm) from the light incident point facilitated accurate estimation of μ_s' and μ_a in 5 mm diameter blood vessels located 1 mm below the body surface.

6. Conclusions

For noninvasive measurement of blood turbidity from the body surface, a technique was developed to enable measurement of the optical properties of blood within subcutaneous blood vessels. Our approach is based on the diffusion approximation of the radiative transfer equation, thereby enabling estimation of the effective attenuation coefficient μ_{eff} of a turbid medium through space-resolved reflectance measurements along the medium surface. Based on analytical equations, we obtained the reduced scattering coefficient μ_s' and the absorption coefficient μ_a from μ_{eff}. To accommodate non-scattering-dominant media such as blood, we introduced a modified diffusion coefficient in the equations. To determine both μ_s' and μ_a, we employed a two-wavelength reflectance measurement, thereby enabling the formulation of two simultaneous equations for the unknowns μ_s' and μ_a. We proposed a convenient process for solving these equations. In this solution process, we can directly validate the reasonability of the solutions, thereby preventing the occurrence of non-significant or erroneous outcomes.

In conclusion, this study presents an innovative technique for estimating the localized optical properties in a turbid medium. It offers a new tool for noninvasive monitoring of optical properties of blood within subcutaneous blood vessels. We have demonstrated its validity and limitations through extensive analyses. However, all these analyses are based on simulations and are not exempt from their limitations. Ultimately, they must be demonstrated through experimentation. Verification of its practical usefulness in real-world applications also remains an area for future research with animal experiments.

Separate estimation of scattering and absorption coefficients from a reflectance measurement will provide a useful tool for the noninvasive monitoring of subsurface structures in various domains. Overall, the proposed technique holds considerable potential in various biomedical applications.

Disclosures. The authors declare no conflicts of interest.

Data availability. Data underlying the results presented in this paper are not publicly available at this time but may be obtained from the authors upon reasonable request.

References

1. J. G. Webster, "*The Physiological Measurement Handbook*," CRC Press (2014).

2. J. Serup, G. B. E. Jemec, and G. L. Grove, eds., *Handbook of Non-Invasive Methods and the Skin*, 2nd ed., CRC Press (2006).

3. P. Gloviczki, M. C. Dalsing, B. Eklof, *et al.*, eds. *Handbook of Venous and Lymphatic Disorders*, 4th ed., CRC Press (2017).

4. V. Tuchin, *Tissue Optics: Light Scattering Methods and Instruments for Medical Diagnosis*, 3rd ed. (SPIE Press, 2015).

5. D.A. Boas, C. Pitris, and N. Ramanujam, *Handbook of Biomedical Optics* (CRC Press, 2011).

6. R. Splinter and B.A. Hooper, *An Introduction to Biomedical Optics*, (Taylor and Francis, 2007).

7. T. Vo-Dinh, *Biomedical Photonics Handbook* (CRC Press, 2003).

8. D. Lairon, J. Lopez-Miranda, and C. Williams, "Methodology for studying postprandial lipid metabolism," Eur. J. Clin. Nutr. **61**(10), 1145–1161 (2007).

9. A. Helkin, J. J. Stein, S. Lin, *et al.*, "Dyslipidemia Part 1—Review of Lipid Metabolism and Vascular Cell Physiology," Vascular and Endovascular Surgery **50**(2), 107–118 (2016).

10. G. Riccardi, L. Bozzetto, and G. Annuzzi, "Postprandial lipid metabolism," Scandinavian Journal of Food and Nutrition **50**(sup2), 99–106 (2006).

11. J. H. O'Keefe and D. S. H. Bell, "Postprandial hyperglycemia/ Hyperlipidemia (postprandial dysmetabolism) Is a cardiovascular risk factor," Am. J. Cardiol. **100**(5), 899–904 (2007).

12. A. Ceriello and S. Genovese, "Atherogenicity of postprandial hyperglycemia and lipotoxicity," Rev. Endocr. Metab. Disord. **17**(1), 111–116 (2016).

13. N. Rifai, G. R. Warnick, and M. H. Dominiczak, eds., "*Handbook of Lipoprotein Testing*," 2nd eds. (American Association for Clinical Chemistry, 2001).

14. U. Laufs, K. G. Parhofer, H. N. Ginsberg, *et al.*, "Clinical review on triglycerides," Eur. Heart J. **41**(1), 99–109c (2020).

15. D. Lütjohann, H.-U. Klör, and F. Stellaard, "Measurement of Serum Low Density Lipoprotein Cholesterol and Triglyceride-Rich Remnant Cholesterol as Independent Predictors of Atherosclerotic Cardiovascular Disease: Possibilities and Limitations," Nutrients **15**(9), 2202–2202.12 (2023).

16. R. Michels, F. Foschum, and A. Kienle, "Optical properties of fat emulsions," Opt. Express **16**(8), 5907 (2008).

17. K. Iinaga, T. Namita, T. Sakurai, *et al.*, "Attempt for noninvasive evaluation of in vivo triglyceride in blood," *Proc. 35th Annual Int. Conf. of the IEEE EMBS*, p. 1214 (2013).

18. R. Sascău, A. Clement, R. Radu, *et al.*, "Triglyceride-Rich Lipoproteins and Their Remnants as Silent Promoters of Atherosclerotic Cardiovascular Disease and Other Metabolic Disorders: A Review," Nutrients **13**(6), 1774–- 1774-15 (2021).

19. M. S. Patterson, B. Chance, and B. C. Wilson, "Time resolved reflectance and transmittance for the noninvasive measurement of tissue optical properties," Appl. Opt. **28**(12), 2331 (1989).

20. D. J. Durian and J. Rudnick, "Spatially resolved backscattering: implementation of extrapolation boundary condition and exponential source," J. Opt. Soc. Am. A **16**(4), 837 (1999).

21. E. Zherebtsov, V. Dremin, A. Popov, *et al.*, "Hyperspectral imaging of human skin aided by artificial neural networks," Biomed. Opt. Express **10**(7), 3545–3559 (2019).

22. S. Liang and K. Shimizu, "Development of a technique to measure local scattering in turbid media using backscattered light at the surface for noninvasive turbidity – evaluation of blood in subcutaneous blood vessels," Jpn. J. Appl. Phys. **60**(2), 022002 (2021).

23. T. J. Farrell, M. S. Patterson, and B. Wilson, "A diffusion theory model of spatially resolved, steady-state diffuse reflectance for the noninvasive determination of tissue optical properties in vivo," Med. Phys. **19**(4), 879–888 (1992).

24. G. Kumar and J. M. Schmitt, "Optimal probe geometry for near-infrared spectroscopy of biological tissue," Appl. Opt. **36**(10), 2286 (1997).

25. V. Tuchin, *Handbook of Optical Biomedical Diagnostics* (SPIE Press, 2002).

26. D. J. Durian, "The diffusion coefficient depends on absorption," Opt. Lett. **23**(19), 1502–1504 (1998).

27. A. Garofalakis, G. Zacharakis, G. Filippidis, *et al.*, "Characterization of the reduced scattering coefficient for optically thin samples: Theory and experiments," J. Opt. A: Pure Appl. Opt. **6**(7), 725–735 (2004).

28. K. Furutsu and Y. Yamada, "Diffusion approximation for a dissipative random medium and the applications," Phys. Rev. E **50**(5), 3634–3640 (1994).

29. J. Ripoll, D. Yessayan, G. Zacharakis, *et al.*, "Experimental determination of photon propagation in highly scattering and absorbing media," J. Opt. Soc. Am. A **22**(3), 546–551 (2005).

30. L. V. Wang and H.-I. Wu, *Biomedical Optics: Principles and Imaging* (Wiley, 2007).

31. X. Wang, G. Yao, and L. V. Wang, "Monte Carlo model and single scattering approximation of the propagation of polarized light in turbid media containing glucose," Appl. Opt. **41**(4), 792 (2002).

32. M. Friebel, A. Roggan, G. Müller, *et al.*, "Determination of optical properties of human blood in the spectral range 250 to 1100 nm using Monte Carlo simulations with hematocrit-dependent effective scattering phase functions," J. Biomed. Opt. **11**(3), 034021 (2006).

33. A. Roggan, K. Doerschel, O. Minet, *et al.*, "The optical properties of biological tissue in the near infrared wavelength range: review and measurements," in *Laser-Induced Interstitial Thermotherapy* (SPIE Press, Bellingham, WA, 1995).

34. A. N. Bashkatov, E. A. Genina, V. I. Kochubey, *et al.*, "Optical properties of human skin, subcutaneous and mucous tissues in the wavelength range from 400 to 2000nm," J. Phys. D: Appl. Phys. **38**(15), 2543–2555 (2005).

35. S. L. Jacques, "Optical properties of biological tissues: a review," Phys. Med. Biol. **58**(11), R37–R61 (2013).
36. N. Bosschaart, G. J. Edelman, M. C. G. Aalders, *et al.*, "A literature review and novel theoretical approach on the optical properties of whole blood," Lasers Med Sci **29**(2), 453–479 (2014).
37. K. Calabro, "Modeling Biological Tissues in LightTools," Technical Paper of Synopsys, 1–14 (2020).
38. I. V. Meglinsky and S. J. Matcher, "Modelling the sampling volume for skin blood oxygenation measurements," Med. Biol. Eng. Comput. **39**(1), 44–50 (2001).
39. D. Y. Churmakov, I. V. Meglinski, and D. A. Greenhalgh, "Influence of refractive index matching on the photon diffuse reflectance," Phys. Med. Biol. **47**(23), 4271–4285 (2002).
40. V. Dremin, E. Zherebtsov, A. Bykov, *et al.*, "Influence of blood pulsation on diagnostic volume in pulse oximetry and photoplethysmography measurements," Appl. Opt. **58**(34), 9398–9405 (2019).
41. A. Bykov, V. Tuchin, and I. Meglinski, "Multiplexed spatially-focused localization of light in adipose biological tissues," Sci. Rep. **12**(1), 9711 (2022).
42. R. Bays, G. Wagnières, D. Robert, *et al.*, "Clinical determination of tissue optical properties by endoscopic spatially resolved reflectometry," Appl. Opt. **35**(10), 1756 (1996).
43. A. Kienle, L. Lilge, M. S. Patterson, *et al.*, "Spatially resolved absolute diffuse reflectance measurements for noninvasive determination of the optical scattering and absorption coefficients of biological tissue," Appl. Opt. **35**(13), 2304 (1996).